

# JGR Solid Earth



## RESEARCH ARTICLE

10.1029/2020JB020263

### Key Points:

- The 2008 Wells earthquake ruptured the shallow and deep parts of a listric fault
- Near-field USArray data are key to constrain the deep and shallow parts of the rupture
- Teleseismic and geodetic data cannot resolve the shallow part of the rupture

### Supporting Information:

Supporting Information may be found in the online version of this article.

### Correspondence to:

A. M. G. Ferreira,  
A.Ferreira@ucl.ac.uk

### Citation:

Frietsch, M., Ferreira, A. M. G., & Funning, G. J. (2021). Data-driven two-fault modeling of the Mw 6.0 2008 Wells, Nevada earthquake suggests a listric fault rupture. *Journal of Geophysical Research: Solid Earth*, 126, e2020JB020263. <https://doi.org/10.1029/2020JB020263>

Received 28 MAY 2020

Accepted 17 FEB 2021

## Data-Driven Two-Fault Modeling of the Mw 6.0 2008 Wells, Nevada Earthquake Suggests a Listric Fault Rupture

Michael Frietsch<sup>1,2</sup>, Ana M. G. Ferreira<sup>1,3</sup> , and Gareth J. Funning<sup>4</sup> 

<sup>1</sup>Department of Earth Sciences, University College London, London, UK, <sup>2</sup>Now at Geophysical Institute (GPI), Karlsruhe Institute of Technology, Karlsruhe, Germany, <sup>3</sup>CERIS, Instituto Superior Técnico, Universidade de Lisboa, Lisboa, Portugal, <sup>4</sup>Department of Earth and Planetary Sciences, University of California, Riverside, CA, USA

**Abstract** Structural fault complexity at depth affects seismic hazard, earthquake physics, and regional tectonic behavior, but constraining such complexity is challenging. We present earthquake source models of the February 21, 2008, Mw 6.0 Wells event that occurred in the Basin and Range in the western USA, suggesting the rupture of both the shallow and deep parts of a listric fault. We use a large data set including 150 local seismic waveforms from the USArray combined with high-quality Interferometric Synthetic Aperture Radar and teleseismic waveforms. Rather than imposing an a priori fault geometry in the source inversions, as is often done in the literature, we use a data-driven approach whereby all the faulting parameters and number of faults are determined by the data alone. We find a two-fault normal faulting solution comprising: (i) a shallow (centroid depth  $\sim 4.6$  km) sub-event with Mw 5.3 and fault dip of  $\sim 77^\circ$ ; and (ii) a deeper (centroid depth  $\sim 8.8$  km), larger Mw 6.0 sub-event on a fault with shallower dip angle ( $\sim 41^\circ$ ). Our preferred two-fault model is consistent with aftershocks and with the tectonics of the region. The local USArray waveforms used in the modeling are key to detect the rupture of both shallow and deep parts of the possible listric fault. The lack of such dense and uniform coverage of earthquakes in other regions on Earth may explain why the full seismic rupture of listric faults may have gone undetected in the past. Thus, earthquake slip on whole listric faults may be more common than previously thought.

**Plain Language Summary** The role of fault complexity on the earthquake source process remains debated. An example of such complexity includes so-called listric faults, which are curved faults whose curvature decreases with depth. While these faults are common worldwide, it is not clear whether earthquakes rupture whole listric fault structures or only parts of them. We studied the February 21, 2008, Mw 6.0 Wells, Nevada event that occurred in the Basin and Range in the western USA using a large data set including local and teleseismic waveforms, as well as Interferometric Synthetic Aperture Radar (InSAR) data. We find that the 2008 Wells earthquake ruptured the shallow and deep parts of a possible listric fault. While the teleseismic and InSAR data cannot resolve the shallow part of the rupture, the local seismic data are key to constrain the deep and shallow parts of the rupture. The lack of dense and uniform local data coverage of earthquakes in other regions on Earth may explain why the full seismic rupture of listric faults may have gone undetected in the past. Thus, earthquake slip on whole listric faults may be more common than previously thought.

## 1. Introduction

The role of structural fault complexity on the earthquake rupture process remains debated. Listric normal faults, which are curved faults with a dip angle that decreases with depth resulting in a concave upward profile, are a good example of complex structures at depth that are important in the development of rift valleys, core complexes, salt domes, etc. (e.g., Shelton, 1984). Listric normal faults are common in extensional regions, such as the East African rift, Afar, the Apennines, the Po plain, the Upper Rhine graben and the Basin and Range (Gibbs, 1984; Proffett, 1977; Shelton, 1984; Stewart, 1971; Wernicke & Burchfiel, 1982). Moreover, they are also common secondary extensional features in convergent regions (e.g., McNeill et al., 1997). Listric faults may occur because they reactivate curved thrusts or when brittle rocks overlie ductile rocks in an extensional regime (e.g., Shelton, 1984). Their curvature is thought to be linked to the rotation of beds (e.g., Wernicke & Burchfiel, 1982). A possible explanation for these rotations is the variation of rheology

© 2021. The Authors.

This is an open access article under the terms of the [Creative Commons Attribution](https://creativecommons.org/licenses/by/4.0/) License, which permits use, distribution and reproduction in any medium, provided the original work is properly cited.

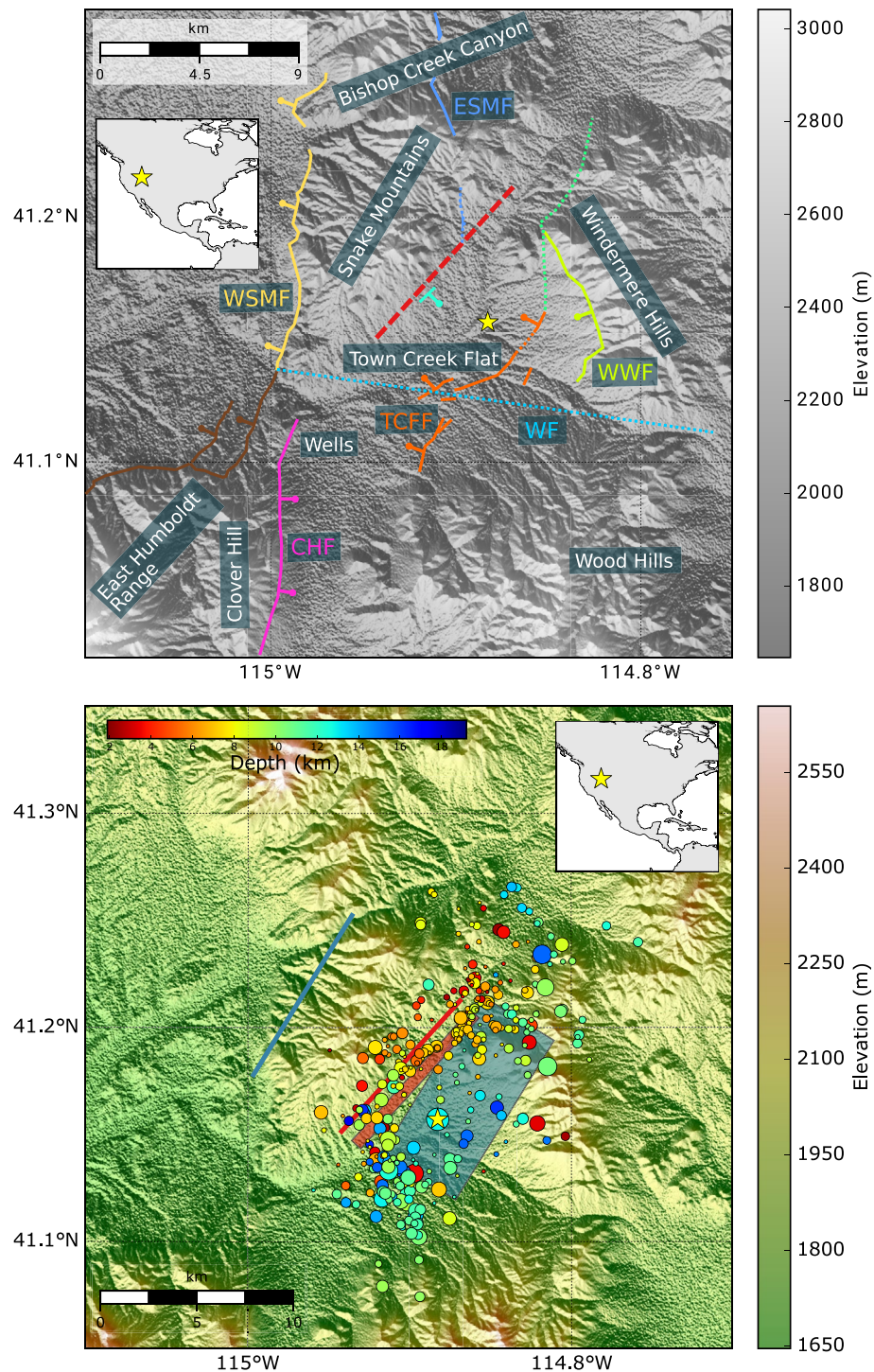
with depth, where brittle faulting in the upper crust generates less rotation than fault creep in the lower part of the crust (Jackson & McKenzie, 1983). However, it is not clear whether earthquakes rupture whole listric fault structures or only parts of them, notably their deeper, shallower-dipping components. Some seismic studies based on first motion analysis (e.g., Doser & Smith, 1989; Jackson & White, 1989) and on down-dip sub-event seismic waveform inversions (e.g., Braunmiller & Nabelek, 1996) suggested that listric normal faults do not rupture seismically along their full down-dip widths. On the other hand, some seismic and geodetic studies suggested the full rupture of listric faults (e.g., Cakir & Akoglu, 2008; Senturk et al., 2019). However, a listric fault configuration was imposed in those studies as a priori information without verifying whether the data used actually require such a configuration. Knowing whether earthquakes rupture whole or only parts of listric faults has important seismic hazard implications, since simulations suggest that fault listricity could have an important effect on peak ground velocities (Passone & Mai, 2017). As listricity increases, the peak ground velocity in the hanging wall increases and enhances constructive interference effects. The latter can double seismic wave amplitudes compared to those generated by a planar fault (Passone & Mai, 2017).

On 21 February 2008, a Mw 6.0 normal faulting earthquake occurred in Wells, Nevada, in the Basin and Range tectonic province in the western USA (Smith et al., 2011). This intraplate event occurred on an unmapped fault segment, filling the gap between the Town Creek section of the Clover Hills fault and the Eastern Snake Mountains fault further North (Henry & Colgan, 2011; Ramelli & dePolo, 2011, Figure 1). The event had a maximum Modified Mercalli Intensity of VIII at Wells (dePolo & Pecoraro, 2011) and caused significant damage in the town of Wells, where seven houses and buildings were destroyed, more than 100 buildings were damaged (dePolo, 2011; dePolo & Pecoraro, 2011) and three people were injured (dePolo & Lotspeich, 2011). Previous studies of this event used seismic and InSAR data to determine a normal faulting mechanism with fault strike between  $19^\circ$  and  $35^\circ$ , fault dip in the range  $33^\circ$ – $41^\circ$  and moment magnitude Mw 5.8–6.2 (Dreger et al., 2011; Mendoza & Hartzell, 2009; Nealy et al., 2017). However, existing source models of the event show discrepancies, notably regarding slip at depth (see Table 1 with solutions from previous studies). Mendoza & Hartzell (2009) used local seismic data to find that the earthquake slipped mainly between 6.5 and 10.8 km depth. On the other hand, Dreger et al. (2011) found shallower slip when using InSAR data (at  $\sim 5$  km depth). Moreover, Nealy et al. (2017) reported that including InSAR data in the source inversions led to shallower slip ( $\sim 7.4$  km) than when using a fault geometry inferred from the aftershocks, with slip at  $\sim 11.5$  km depth. Figure 1 shows the area around the Wells earthquake together with the aftershocks located by Smith et al. (2011). While previous studies considered that the Wells earthquake occurred on a single planar fault, the aftershock distribution of Smith et al., 2011 suggests a listric fault configuration (see the Movie S1 in the supporting information). In addition, the GCMT and USGS moment tensor solutions of the event estimate non-double-couple components of  $\sim 17\%$ – $45\%$  (Table 1), which suggests source complexity.

The Wells earthquake occurred right in the center of the region where the USArray (Transportable Array) was deployed at the time of the event, providing excellent dense seismic coverage. Moreover, it was also captured by multiple tracks of very high-quality InSAR data from the Envisat satellite. Here, we present models of the Wells earthquake built from simultaneous inversions of seismic and InSAR data whereby all faulting parameters and the number of faults are determined by the data alone, without imposing any a priori fault geometry. We show that the data require the seismic rupture of two fault planes suggesting a listric fault and discuss its implications.

## 2. Data

We use the following independent data types to model the Wells earthquake: (i) ascending and descending SAR interferograms obtained from radar satellite images of the ASAR (Advanced Synthetic Aperture Radar) sensor of the Envisat satellite; (ii) 150 local seismic waveforms recorded by the Earthscope Transportable Array (USArray) and permanent stations in the Western USA; and (iii) teleseismic waveforms (49 P-, 49 S-, and 46 surface waveforms) from regional and global seismic networks.



**Figure 1.** Tectonic setting of the Mw 6.0, February 21, 2008 Wells earthquake in Nevada, USA. Top: Quaternary faults and topographic features around the Town Creek Flat region. The colored solid lines are mapped faults, the dotted lines are concealed, while the red dashed line marks the surface projection of the shallower fault obtained from our two-fault joint data inversion. The yellow star marks the epicenter of the mainshock. The faults shown are: ESMF (Eastern Snake Mountain Fault), WSMF (Western Snake Mountain Fault), TCFF (Town Creek Flat Fault), WWF (West Windermere Fault), WF (Wells Fault) and CHF (Clover Hill Fault). The faults are based on the geological map of the Wells area and the GIS data of Henry and Colgan (2011) and from Ramelli and dePolo (2011). Bottom: Surface projection of the two fault planes determined in this study (red and blue rectangles). The circles are the relocated aftershocks of Smith et al. (2011) color-coded according to their depth. The topography is based on the Shuttle Radar Topography Mission Global one arc second elevation model (NASA JPL, 2013). The inset shows the location of the earthquake in relation to the Americas. CHF, Clover Hill Fault; ESMF, Eastern Snake Mountain Fault; TCFF, Town Creek Flat Fault; WF, Wells Fault; WSMF, Western Snake Mountain Fault; WWF, West Windermere Fault.

**Table 1**

Source Parameters for the  $M_w$  6.0, February 21, 2008 Wells, Nevada Earthquake From Different Agencies (GCMT and USGS), and From Different Published studies

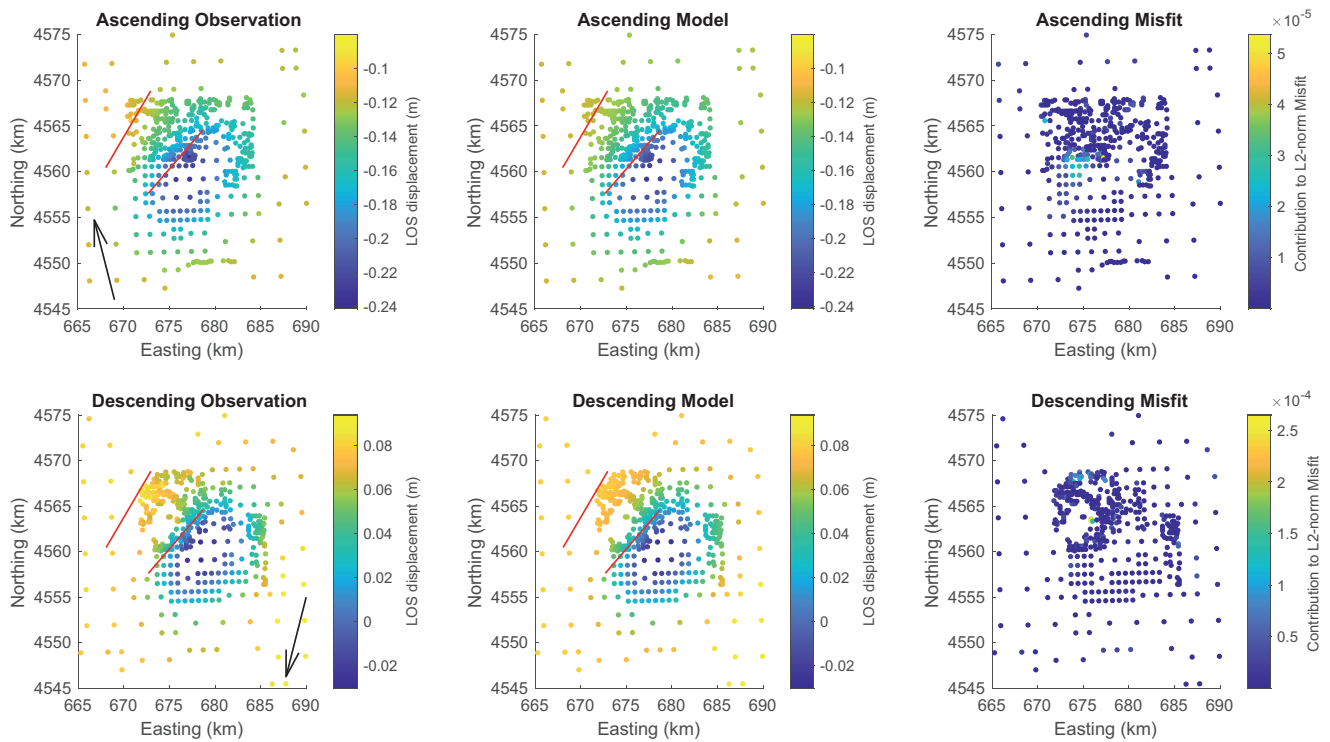
| Agency/study                                 | Strike (°) | Dip (°) | Rake (°) | Depth (km) | DC (%) | $M_w$ |
|--|------------|---------|----------|------------|--------|-------|
| GCMT   | 30         | 40      | −86      | 13.5       | 84     | 6.0   |
| USGS W-Phase                                 | 26         | 41      | −97      | 11.5       | 83     | 6.0   |
| USGS BMT                                     | 19         | 33      | −96      | 7.0        | 55     | 5.8   |
| Local BMT (Dreger et al., 2011)              | 35         | 40      | −82      | 7          | -      | 5.9   |
| DS Local BMT (Dreger et al., 2011)           | 35         | 40      | -        | ~10        | -      | 6.0   |
| DS EGF (Mendoza & Hartzell, 2009)            | 36         | 44      | -        | ~8.5       | -      | 5.8   |
| DS InSAR, aftershock (Dreger et al., 2011)   | 40         | 55      | -        | ~5         | -      | 6.1   |
| DS seismic, aftershock (Dreger et al., 2011) | 40         | 55      | -        | ~8         | -      | 6.0   |
| DS InSAR (Nealy et al., 2017)                | 25         | 41      | -        | 7.4        | -      | 6.2   |
| DS InSAR, aftershock (Nealy et al., 2017)    | 20         | 35      | -        | 11.5       | -      | 6.1   |

The values for fault strike, fault dip, fault rake, fault depth, double couple component (“DC”), and moment magnitude ( $M_w$ ) are reported. The fault depth describes either the centroid depth for the moment tensors, or the average slip of the distributed slip inversions (depths marked with a ~ symbol show the average slip depth estimated from figures in the respective studies because the depth values are not directly reported). “Local BMT”: moment tensor study of Dreger et al. (2011) based on local seismic data; “DS Local BMT”: distributed slip solution obtained from local seismic data imposing the fault geometry obtained from a body wave moment tensor inversion (Dreger et al., 2011); “DS EGF”: distributed slip solution obtained from an Empirical Green’s Function approach (Mendoza & Hartzell, 2009); “DS InSAR, aftershock”: distributed slip solution obtained from InSAR data, with the fault geometry from aftershock relocations (Nealy et al., 2017); “DS seismic, aftershock”: distributed slip solution from local seismic data (Dreger et al., 2011) based on the fault geometry inferred from aftershocks of Smith et al. (2011); “DS InSAR”: distributed slip solution obtained from InSAR data (Nealy et al., 2017).

Abbreviations: InSAR, Interferometric Synthetic Aperture Radar.

## 2.1. InSAR Data

The Envisat satellite had a repeat interval of 35 days between radar images acquired on the same orbital track. The ASAR sensor operated in the C-band with a wavelength of 5.6 cm. The ascending image pair (track 220, with the acquisition on November 14, 2007 and April 02, 2008) and descending image pair (track 399, acquisition on August 13, 2007 and April 13, 2008) are processed with the software package InSAR Scientific Computing Environment (ISCE, Agram et al., 2013). Two additional InSAR tracks were available from Envisat (tracks 127 and 492), but the data were either very noisy (track 127) or covered a too long time interval (track 492), and hence we did not use them. In any case, the minor differences in incidence angle permitted by these additional tracks would be unlikely to significantly improve our resolution of the deformation field for the Wells earthquake (e.g., Wright et al., 2004). The 1 arc-second Shuttle Radar Topography Mission (SRTM) digital elevation model (Farr et al., 2007; NASA JPL, 2013) is used to remove the topographic phase and to geocode the InSAR data. The phase is unwrapped with Statistical-cost Network-flow Approach for Phase Unwrapping (SNAPHU; Chen and Zebker, 2001). In order to reduce the computational cost of the analysis, the Line Of Sight (LOS) displacements are downsampled using a quadtree decomposition (e.g., Funning et al., 2005; Jonsson, 2002; Weston et al., 2014). Consequently, the downsampled interferogram for the ascending track consists of 633 data points and of 599 data points for the descending track (Figure 2). In order to remove orbital errors and subsequent long-wavelength phase ramps in the interferograms, three additional parameters for each geodetic data set are solved for in the inversion process and removed from the data: a translation (static offset) in the radar line-of-sight, as well as two linear gradients in the north and east directions. As explained in the Results section below, we found an excellent agreement between the observed InSAR data and the predictions from the co-seismic deformation. We would expect that any unmodelled postseismic deformation that would be present in the InSAR data would lead to systematic residuals in the same place in the ascending and descending interferograms, which do not appear in our results. GPS data coverage is limited in the area, but there is at least one station triplet shown by Hammond et al. (2014) that has a co-seismic offset due to the Wells earthquake, but no nonlinear



**Figure 2.** InSAR data set of the Envisat satellite for ascending track 220 with 633 data points zoomed in on the fault area (top row) and descending track 399 with 599 data points (bottom row): (a), (d) Observed Line of Sight (LOS) displacement; (b), (e) Modeled LOS displacement; (c), (f) the contribution to the L2-norm misfit, which is dimensionless. The red lines mark the projected surface breakout of the two faults shown in Figure 1 in the main text. The flight direction of the right-looking Envisat satellite is shown by the black arrow. The models and the misfit relate to solutions from the joint inversion of local waveforms, teleseismic and InSAR data. For completeness, Figure S1 in the Supporting Information shows all the InSAR data points used. InSAR, Interferometric Synthetic Aperture Radar; LOS, Line of Sight.

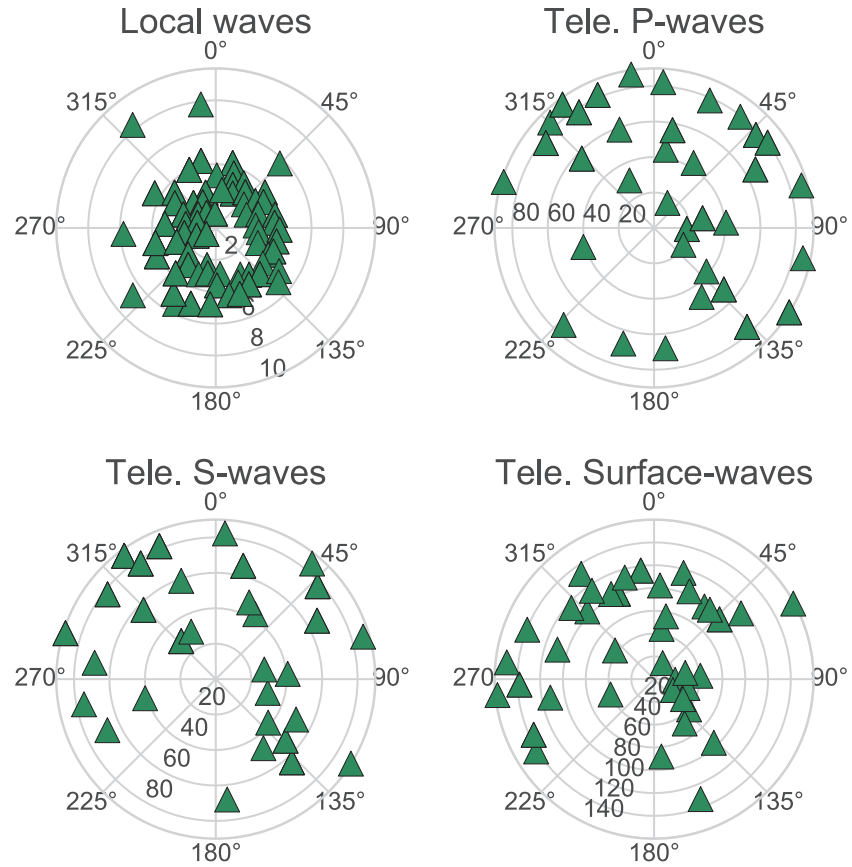
transient following it. On that basis, we have no reason to expect any detectable postseismic deformation in the InSAR data and thus there are no additional corrections accounting for the contribution of post-seismic deformation to the co-seismic InSAR LOS-displacements.

## 2.2. Seismic Data

We use three-component seismic waveforms bandpass filtered in the range  $\sim 17$ – $180$  s, depending on the data type. The filtering parameters are chosen to achieve a good signal-to-noise ratio without substantial loss of information. We select the station with the best signal-to-noise ratio for each  $5^\circ$  azimuthal interval in order to get a balanced azimuthal distribution of the stations (Figure 3). Table S1 in the supporting information shows all the relevant data selection and processing parameters, notably the epicentral distance range and the filtering parameters used. Figure 4 shows illustrative examples of local and teleseismic waveforms (all waveforms are shown in Figures S3–S5). The epicentral distance range of the teleseismic data (see Figure 3) was selected to avoid sampling the complex lowermost mantle with body waves and also to avoid the interference of multiple orbit wave trains. We choose time windows that fully capture each seismic phase. While the windowing of the body waves is based on phase arrivals estimated by the travel time calculator TauP (Crotwell et al., 1999), the maximum of the envelope function is used to select the time window for the teleseismic surface waves.

## 3. Source Inversion Method

We use the simultaneous multiple fault source inversion method of Frietsch et al. (2019) whereby each fault is described by 11 source parameters: fault strike, dip, rake, average slip, length, width, centroid longitude, latitude and depth, the time shift to the centroid time, and the compensated-linear-vector-dipole (CLVD,  $\nu$ )



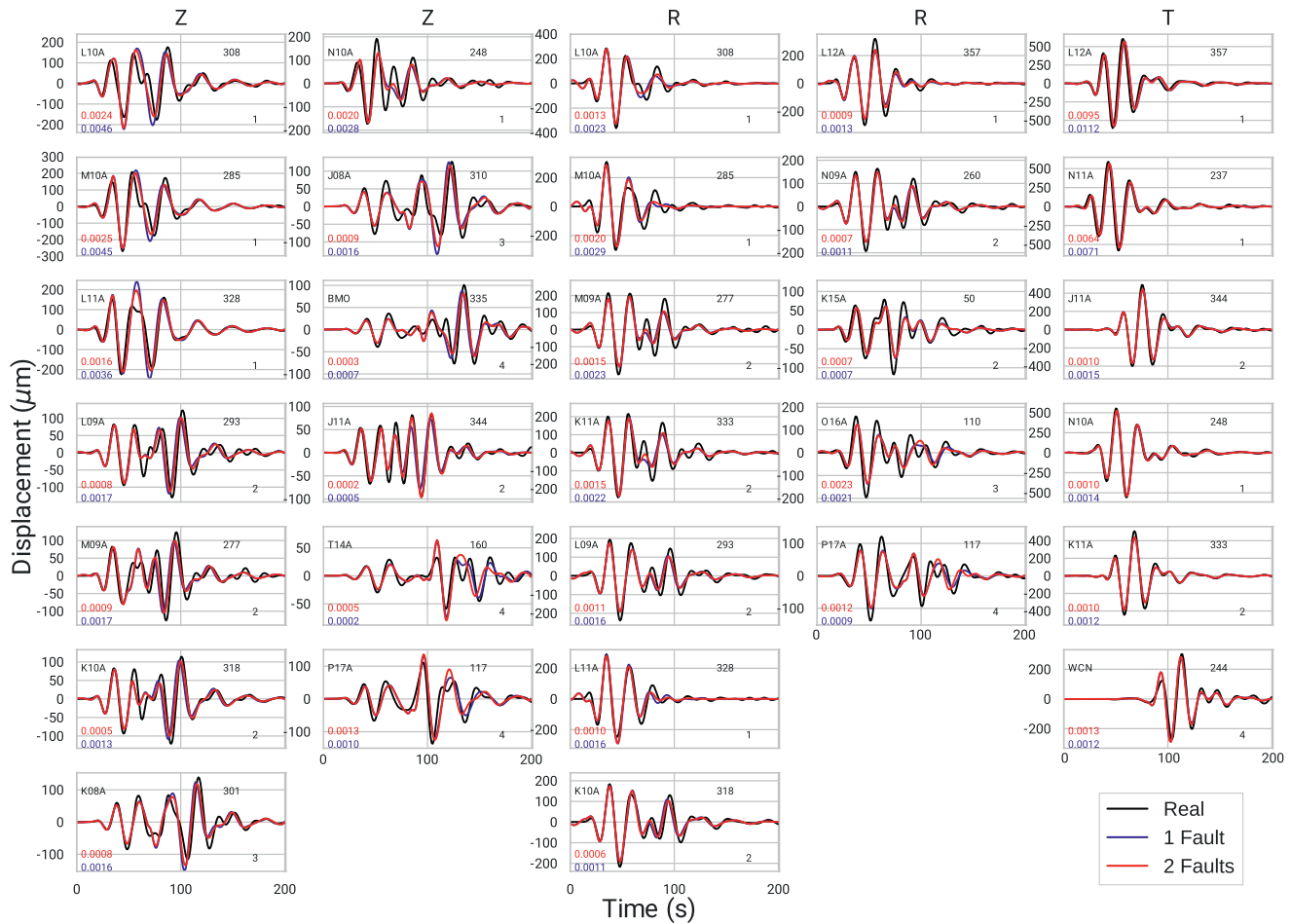
**Figure 3.** Station distribution for the seismic data sets used in this study: local seismic waves (top left); teleseismic surface waves (Top right); teleseismic P waves (bottom left); and, teleseismic S waves (bottom right). The diagrams show the source-receiver azimuth range from 0° to 360° while the radial direction shows the epicentral distance range in degrees.

component, following the approach of Tape and Tape (2015). The  $\nu$  parameter is calculated directly from the moment tensor eigenvalues and is similar to other measures, such as lune longitude  $\gamma$  or the classical  $\epsilon$  parameter (Ekström et al., 2012). While source studies in the literature typically impose a priori fault geometries in the inversions, our approach consists of letting the data alone determine the optimal fault parameters and number of faults. Thus, the search for the source parameters for each fault is totally free within reasonable bounds (Table S2). Our method uses the Powell algorithm (Powell, 1964) as its local optimization scheme in an inversion with multiple Monte Carlo restarts in order to find the global minimum of the  $L_2$ -norm misfit. The misfit function  $m^2$  is based on the difference between the theoretical seismograms  $t_s$  and the observed seismograms  $d_s$ , as well as the difference between the theoretical geodetic  $t_G$  and observed geodetic  $d_G$  displacements with weighting factors for the seismic and geodetic components given by  $\alpha_s$  and  $\alpha_G$ , respectively:

$$m^2 = \alpha_s \frac{(t_s - d_s)^T (t_s - d_s)}{d_s^T d_s} + \alpha_G \frac{(t_G - d_G)^T (t_G - d_G)}{d_G^T d_G} \quad (1)$$

The number of restarts of the algorithm depends on the complexity of the source model. Having extensively experimented with the number of restarts and iterations, we found that 200 to 1,000 Monte Carlo restarts are enough for a single planar fault model to converge, while a two-fault model needs at least 100,000 iterations.

The InSAR displacements are modeled using elastic dislocation theory for the displacement of a rectangular fault in a homogeneous half-space (Okada, 1985) assuming a constant shear modulus  $\mu = 30$  GPa and














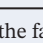
**Figure 4.** Illustrative examples of local seismic waveforms from the Mw 6.0, February 21, 2008 Wells, Nevada earthquake (all waveforms are shown in Figure S3). The observed data are in black, the best-fitting synthetics from joint inversion of local waveforms, teleseismic and InSAR data are in blue (single fault solution) and in red (two-fault solution). Each subplot shows the station name in the top left corner, the azimuth in the top right and the epicentral distance in degrees in the bottom right. The contribution to the overall data misfit  $m^2$  (Equation 1) is also shown for each individual trace on the bottom left for the single fault solution (blue) and for the two-fault solution (red). Specifically, the numerator in Equation 1 is only computed for the seismic trace considered while the denominator is computed over all the seismic traces. A Butterworth bandpass filter in the range from 16.6 to 33.3 s is used. The traces are sorted across the columns by decreasing difference in misfit between the single fault and the two-fault solutions. InSAR, Interferometric Synthetic Aperture Radar.

corresponding to a pure double-couple source model. Following Weston et al. (2014), the seismic centroid location is fixed to the center of the fault plane obtained from single fault inversions using only InSAR data.

Using the centroid location obtained from the inversions of InSAR data, synthetic seismograms and seismic sensitivity kernels for source parameters are computed with the highly accurate spectral element method, using the SPEC-FEM3D\_GLOBE package (Komatitsch & Tromp, 2002). The global 3-D whole mantle shear wave model SGLOBE-rani (Chang et al., 2015) is employed combined with the CRUST2.0 (Bassin et al., 2000) crustal model. Despite being relatively expensive computationally, given the linear relationship between the moment tensor and the seismic waveforms, sensitivity kernels are pre-computed for the centroid location obtained from the InSAR data and stored before being used in the source inversions.

Model uncertainties are estimated using a heuristic approach, by defining error bounds based on the source models that fit the data within 20% of the minimum misfit value. This misfit threshold value was chosen such that the corresponding models all fit the data reasonably well. First, the different seismic and geodetic data sets are inverted separately to explore their sensitivity to the different source parameters. Then, the weighting factors ( $\alpha_S$  and  $\alpha_G$ ) in the joint data inversions are adjusted to give a similar importance to each data set (see Frietsch et al., 2019 for further details).

**Table 2**  
Inversion Results for the Mw 6.0 February 21, 2008, Wells Nevada Earthquake

| Inv. type | Faults | Fault Nr | Strike (°) | Dip (°) | Rake (°) | DC (%) | $\nu$   | Time lag (s) | Misfit | $M_0$ (N.m) $\times 10^{18}$ | $M_w$ | Stereo  |
|-----------|--------|----------|------------|---------|----------|--------|---------|--------------|--------|------------------------------|-------|---|
| Local     | 1      | 1        | 30.5       | 41.2    | −89.6    | 97     | −0.0094 | −2           | 0.20   | 1.2                          | 6.0   |    |
| Local     | 2      | 1        | 24.7       | 63.2    | −91.3    | 45     | 0.2405  | 14           | 0.17   | 0.24                         | 5.5   |    |
| Local     | 2      | 2        | 30.6       | 40.0    | −89.3    | 97     | 0.0091  | −2           | 0.17   | 1.2                          | 6.0   |    |
| Tele      | 1      | 1        | 30.4       | 41.9    | −89.3    | 94     | −0.0225 | −3           | 1.07   | 1.1                          | 6.0   |    |
| Tele      | 2      | 1        | 180.0      | 62.5    | −75.5    | 93     | −0.0287 | 5            | 0.97   | 0.74                         | 5.8   |    |
| Tele      | 2      | 2        | 53.5       | 55.4    | −80.6    | 16     | −0.3206 | −1           | 0.97   | 0.85                         | 5.9   |    |
| InSAR     | 1      | 1        | 33.9       | 41.2    | −88.0    | 100    | 0       | −            | 0.009  | 1.2                          | 6.0   |    |
| InSAR     | 2      | 1        | 35.4       | 85.3    | −125.4   | 100    | 0       | −            | 0.007  | 1.2                          | 6.0   |    |
| InSAR     | 2      | 2        | 33.6       | 17.5    | −76.0    | 100    | 0       | −            | 0.007  | 1.3                          | 6.0   |    |
| Joint     | 1      | 1        | 31.6       | 41.5    | −89.0    | 93     | −0.0270 | −2           | 2.21   | 1.1                          | 6.0   |    |
| Joint     | 2      | 1        | 40.8       | 77.3    | −90.3    | 99     | 0.0011  | 13           | 2.09   | 0.12                         | 5.3   |  |
| Joint     | 2      | 2        | 30.4       | 41.0    | −89.9    | 93     | −0.0280 | −2           | 2.09   | 1.1                          | 6.0   |  |

Single fault solutions are represented by a blue beach ball, while two-fault solutions are shown with red beach balls. The fault parameters shown are the fault strike, dip, rake, the double-couple Percentage (“DC”), the CLVD  $\nu$  component (Tape & Tape, 2015), the time lag to the GCMT time, the seismic moment, the moment magnitude, the  $L_2$ -norm misfit (Equation 1; see details in the main text) and the corresponding stereonet plot. We compute the non-double-couple ( $\epsilon$ ) percentage of the solutions from the eigenvalues  $\lambda_i$  of the moment tensor using the same approach as e.g. in the GCMT catalog:  $\epsilon = 100 \times \min(|\lambda_i|)/\max(|\lambda_i|)$  (Ekström et al., 2012), with the double-couple component being  $DC = 100 - \epsilon$ . We report solutions obtained with various subsets of data whereby “Local” refers to local seismic data (with Epicentral distance smaller than 10°), “Tele” refers to teleseismic data (with Epicentral distance between 30° and 140°), “InSAR” refers to the use of InSAR data alone and “Joint” refers to joint data inversions combining the local, teleseismic and InSAR data.

Abbreviations: InSAR, Interferometric Synthetic Aperture Radar.

The multiple fault inversion scheme successively adds subfaults to the modeling as required by the data. Every source inversion starts by considering a single fault. The number of subfaults is then increased one by one until the improvement in data misfit is smaller than 5% or if the moment magnitude of the additional sub-event becomes smaller than the previous one by one magnitude unit or more. The 5% threshold in the data misfit criteria is consistent with previous seismic studies that used similar thresholds taking data noise into consideration (e.g., Debayle & Ricard, 2012; Parisi & Ferreira, 2016). After performing extensive inversions, we found that once three-fault models were considered, they led to marginal improvements in the data fit (smaller than 5%) compared to two-fault models. Hence, in this study we take the conservative approach of focusing on simpler one- and two-fault models.

#### 4. Results

Table 2 and Figure 1 show the results from single fault and two-fault source inversions of the Wells earthquake. As expected, all the solutions show predominantly normal faulting mechanisms with moment magnitude Mw 6.0. The two-fault solution from the joint data inversion shows a change in fault dip angle from  $\sim 77^\circ$  at shallow depth ( $\sim 5$  km) to  $\sim 41^\circ$  at greater depth ( $\sim 9$  km). It also shows that the earthquake started with a deeper, larger magnitude (Mw  $\sim 6.0$ ) sub-event and extended upwards, with the second shallower,



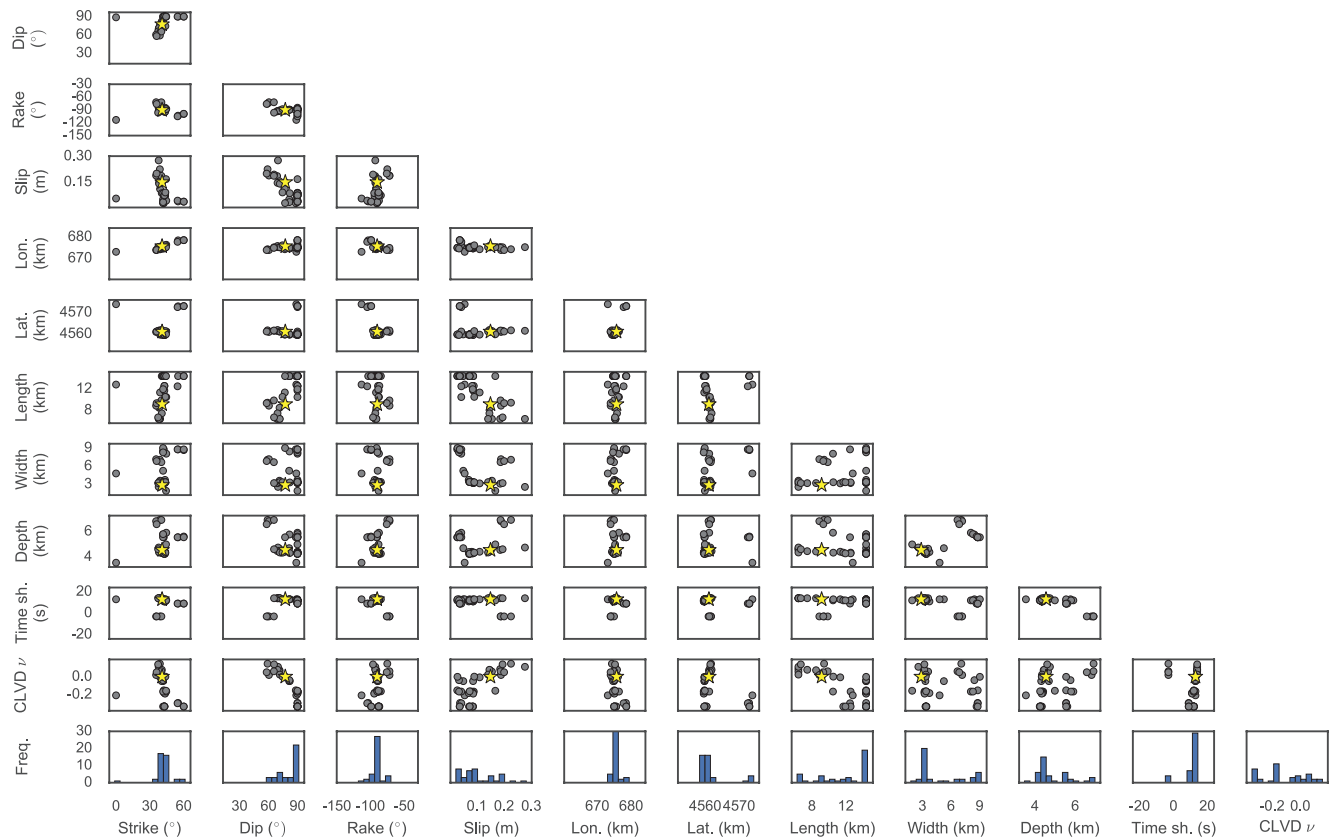
smaller magnitude ( $M_w \sim 5.3$ ) sub-event occurring about 15 s later. This agrees well with the results of Smith et al. (2011), which suggested an earthquake nucleation deeper than the event's aftershocks (Figure 1, Movie S1). Apart from the teleseismic source inversions, the differences between the retrieved fault strike values for the two sub-events do not exceed  $\sim 10^\circ$ . This is within the expected error range for fault strike estimations from source inversions (e.g., Weston et al., 2011, 2012), suggesting that the two sub-events ruptured the same curved fault.

Our source models provide a very good fit to the data, with low waveform misfits (Figures 2, 4 and S3–S5 in the supporting information). The final part of the waveforms occasionally show slightly poorer data fits, which is probably due to inaccuracies in the crustal model used in the forward modeling. When going from a single fault model to a two-fault configuration, the local seismic data show the most substantial improvement in data fit of  $\sim 15\%$  (Table 2), well above the 5% data misfit threshold explained in Section 3. When visually comparing the waveform fits of the single and two-fault models it is not very easy to assess the improvements in data fit mostly due to the large magnitude difference between the two sub-events, which leads to the signal of the smaller magnitude sub-fault being partly covered by the signal of the larger magnitude sub-fault. Nevertheless, we can see clear misfit improvements for example for the vertical components of stations L10A, L11A, and K10A in Figure 4. This is consistent with synthetic inversion tests that showed that InSAR and teleseismic data (i.e., without local data) cannot distinguish two normal sub-faults with down-dip segmentation where one of the sub-events is an order of magnitude smaller than the other (Frietsch et al., 2019). Indeed, the two-fault solutions from teleseismic and InSAR inversions presented in Table 2 only show some slight improvements in data fit compared to the one-fault solutions and show some unlikely features. This includes large differences in fault strike between the two sub-events ( $\sim 127^\circ$ ) for the teleseismic inversions and a difference of  $\sim 40^\circ$  in rake for the InSAR-only solutions. In addition, one of the sub-events obtained from the inversion of teleseismic data alone has a strong, non-double-couple component. This is unlikely since it would suggest non-shear deformation, and it must instead be due to instabilities in the inversions as found, for example, by Frietsch et al. (2018) in inversions of other moderate magnitude events. Moreover, the InSAR data inversion predicts right lateral oblique slip for the upper section and left-lateral oblique slip for the lower section of the fault, which is also improbable. This illustrates the difficulties of the InSAR and teleseismic data in resolving the second, lower magnitude sub-event. Although it may sound counter-intuitive that the InSAR data are not able to discriminate the shallow sub-event, Frietsch et al. (2019) showed that this is due to the event's normal faulting geometry, whose displacements are hard to constrain with InSAR when the event's magnitude is relatively low. This would not be a problem if the earthquake had e.g. a strike-slip faulting mechanism, as the fault segments would be spatially separated in map view, rather than superposed.

In order to test the significance of the differences in data misfit between the single and two-fault models obtained from the joint data inversions, we performed a F-test by computing: 
$$F = \frac{[\chi^2(r) - \chi^2(p)] / (p - r)}{\chi^2(p) / (n - p)},$$

where  $\chi^2$  is the misfit function,  $n$  is the number of data points used in the inversions, and  $p$  and  $r$  are the numbers of model parameters for the two models which are compared ( $p > r$ ). Under the null hypothesis that the two-fault model does not provide a significantly better fit than the single fault model, the null hypothesis is rejected if  $F$  is greater than the critical value of the F-distribution for a given desired false-rejection probability  $P$  (Bevington & Robinson, 2002). Since errors in the data and in the modeling used in our inversions are essentially unknown, here, we use the misfit function  $\chi^2$  based on the  $L_2$ -norm misfit in Table 2 following, for example, Forsyth (1975) and Ferreira et al. (2019). We find that the probability that the improved fit of the two-fault model compared to the single fault model occurs by chance is less than 1% (i.e., the two models differ at the  $P = 0.01$  level). Thus, the F-tests support the significance of the improved data fit of the two-fault model. Moreover, we also tested our source model against independent data, that is, data not used in the inversions, such as, for example, station ELK, which is a near nodal station at an epicentral distance of  $\sim 0.5^\circ$ . We found that when considering the source parameter uncertainties, the corresponding synthetic waveforms fit ELK's data well (see Figure S12).

Figures 5 and 6 show parameter trade-off plots for the 40 best-fitting solutions from our joint source inversions and Table S3 shows the estimated uncertainties from our inversions. As expected, the source parameters are better constrained for the larger magnitude sub-event (Figure 5) than for the lower mag-



**Figure 5.** Trade-off plot for two-fault inversion of the joint local, teleseismic and InSAR data sets. The source parameters of the best-fitting 40 solutions for fault one are shown with gray circles. The yellow star marks the solution with the lowest data misfit. The parameters shown are the  $L_2$ -norm misfit (Equation 1), the fault strike, dip, rake, average slip, centroid longitude and latitude (for UTM zone 11T), fault length, width, the centroid depth of the fault, the time shift to the GCMT time and the compensated-linear-vector-dipole component (CLVD). CLVD, compensated-linear-vector-dipole component; InSAR, Interferometric Synthetic Aperture Radar.

nitude sub-event (Figure 6), which is also consistent with the likely artificial lower double-couple component of this latter event obtained from the inversion of the local seismic data alone (Table 2). The trade-off plots from inversions based on teleseismic or InSAR data individually (Figures S8–S11) show less tightly clustered solutions than when using local seismic data and/or the joint data sets (Figures 5, 6, and S6–S7). Moreover, the uncertainties obtained from the individual data inversions are larger than from the joint data inversions. This highlights the limited power of teleseismic and InSAR data at resolving the two sub-events and the importance of combining complementary data sets. Local seismic data (Figures S6–S7) have a stronger sensitivity to the time shift than teleseismic data (Figures S8–S9). In addition, the inversions based solely on teleseismic data lead to well-known trade-offs between the seismic moment and the fault dip as well as between the seismic moment and the fault rake. The good sensitivity to the location is a strength of the InSAR data set; thus, the events' latitude and longitude are well constrained (Figures S10–S11). Finally, we note that as part of our source inversion tests we also performed source inversions imposing a pure double couple constraint and found that the solutions from the joint data inversions were very similar to those reported in this study.

## 5. Discussion

Figure 7 shows a good agreement between the two-fault solution obtained in this study and the relocated aftershocks of Smith et al., 2011. For completeness, we also compare our solution to the relocated aftershocks of Nealy et al. (2017), which also shows a reasonable agreement albeit slightly poorer than with Smith et al. (2011) (Figure S2 in the supporting information). Nevertheless, we prefer to focus our comparison on the aftershocks obtained by Smith et al. (2011) because they used local data from a dedicated dense net-

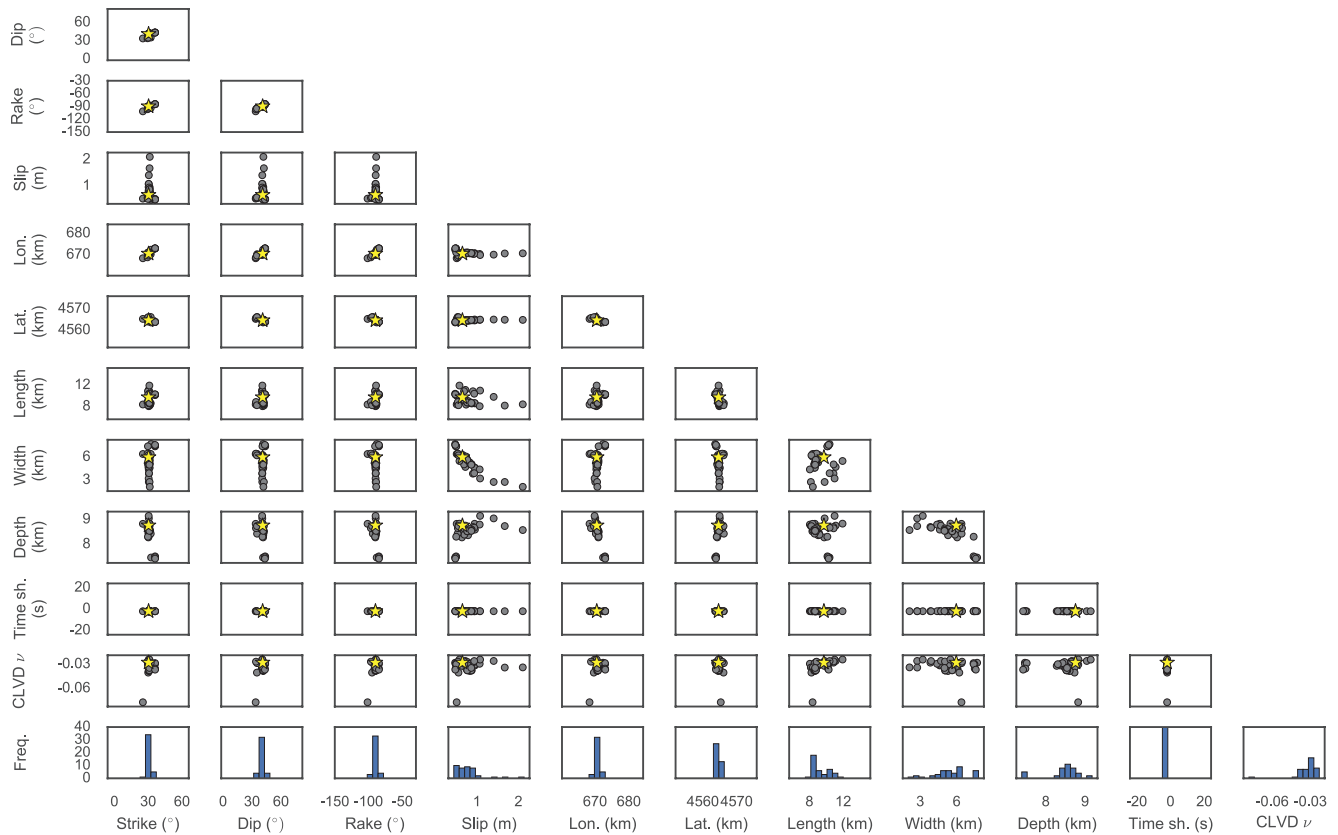
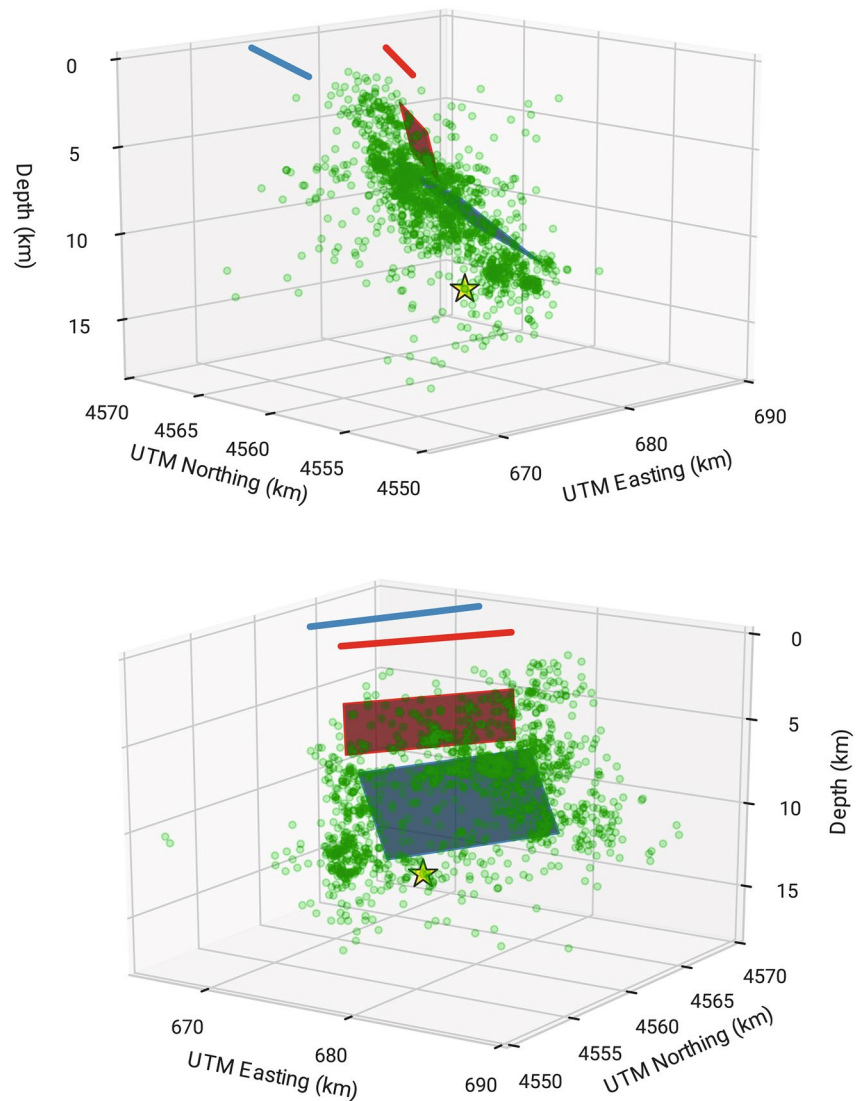


Figure 6. Same as in Figure 5, but for the second fault.

work of 27 temporary stations deployed around the epicenter. On the other hand, Nealy et al. (2017) used primarily USArray stations, only correcting their depth estimates with arrival times from the local stations. While both previous studies of Smith et al. (2011) and Nealy et al. (2017) mention the possibility that the 2008 Wells earthquake may have occurred on a listric fault, neither study tested this possibility. The two-fault model we present here shows slip both at shallow (3.2–6.0 km depth) and greater depths (6.8–10.7 km depth), resolving the depth discrepancy of previous studies e.g., between Dreger et al. (2011) and Nealy et al. (2017). Amongst other techniques, these studies used distributed slip inversions, which can be highly non-unique (e.g., López-Comino et al., 2015). The multiple fault inversion used in this study is an attractive, data-driven and simpler alternative to robustly constrain earthquake source parameters. When considering the two-fault solution obtained in our study, the surface projection of the shallow sub-fault fills a gap between the Town Creek Flat Fault (TCFF, Figure 1) and the Eastern Snake Mountain Fault (ESMF), while the surface projection of the deep sub-fault is further away into the Snake mountains, which is less geologically plausible. Moreover, Figure 1 shows that, as expected, the aftershocks surround the two imaged sub-faults, corresponding to regions of low slip (e.g., Woessner et al., 2006). This adds further confidence to our two-fault solution. We note that for internal consistency of our inversion algorithm, future work will focus on the use of a layered half-space in the modeling of the geodetic data based on the same local layered structure in the source region as in the 3-D Earth models used in the seismic modeling. Nevertheless, this should not change the main results of the joint source inversions because previous studies showed that using layered models versus homogeneous half-spaces in the geodetic modeling affects mainly the source depth and by no more than about 30% (e.g., Hearn & Bürgmann, 2005; Lohman, 2002; Marshall et al., 1991; Savage, 1987).

Listric faults are common in the Basin and Range and have been imaged with seismic reflection (Anderson et al., 1983). However, up to now it was not entirely clear whether a whole listric fault could rupture (e.g., Braunmiller & Nabelek, 1996; Jackson & White, 1989). For example, Stein and Barrientos (1985) and Ward and Barrientos (1986) tested a listric fault geometry in their studies of the 1983 Mw 6.9 Borah Peak, Idaho



**Figure 7.** Comparison between the aftershock distribution of Smith et al. (2011) and the solution from a two-fault joint inversion of local, teleseismic and InSAR data obtained in this study. Aftershocks are marked by green circles and the hypocenter of the mainshock is marked by a yellow star. The two faults are illustrated by red and blue areas and the lines in corresponding colors mark the projected surface breakout. The black arrows show the slip vector. Top: view along strike. Bottom: view perpendicular to the strike. The top and bottom depths of the two faults are: top 3.15 km, bottom 5.95 km for the lower magnitude sub-event; top 6.80 km and bottom 10.71 km for the other sub-event. We note that the discrepancy of  $\sim 4$  km between the location of the mainshock hypocenter and the modeled fault is within depth errors in source inversions ( $\sim 10$  km when using teleseismic data and  $\sim 6$  km when using regional data; e.g., Weston et al., 2012). Moreover, the observed differences between the hypocenter and our deeper fault plane may also be due to the fact that we model the source's centroid, not the hypocenter, and to the use of a homogeneous elastic half-space in the InSAR data modeling (see the Discussion section). We also note that the best-fitting one-fault solution is very similar to that of the largest magnitude, deeper sub-event in the two-fault solution shown in blue. InSAR, Interferometric Synthetic Aperture Radar.

earthquake, which also occurred in the Basin and Range,  $\sim 340$  km away from Wells. Both studies found that a planar fault was in better agreement with their leveling data set. Other studies focusing on other regions also reported the rupture of entire listric faults, notably in Turkey (e.g., Cakir & Akoglu, 2008; Senturk et al., 2019). However, these studies imposed a listric fault configuration *a priori* in their source inversions and did not verify whether the data actually require such configuration compared to simpler fault systems. In contrast, in this study we let the fault geometry and number of faults be freely determined by the data

alone. Hence, to the best of our knowledge, this is the first time that free source inversions demonstrate that geophysical data require a rupture of both the shallow and deep parts of a two-fault system suggesting a listric normal fault.

The long duration of the local seismic signals observed in this study (Figure 3) was also noticed by Biasi and Smith (2011). While this may be partly caused by thick sediments in the Town Creek Flats (Biasi & Smith, 2011), we find that this is linked to a lower magnitude, shallower sub-event rupturing  $\sim 15$  s after the deeper, main sub-event. We suggest that the second sub-event is due to static triggering and also argue that an alternative explanation, such as unmodelled structural effects, is highly unlikely, as it would be very unusual for structural effects to lead to the exact same azimuthal dependency of the waveforms as in the radiation pattern of the second sub-event. Although the shallower sub-event shows stronger parameter trade-offs (Figures 5 and 6) and larger uncertainties (Table S3) than the deeper, larger magnitude sub-event, their parameter uncertainties obtained from the joint data inversions are not excessive and are comparable to those reported for global earthquakes (Weston et al., 2011, 2012).

The two-fault solution suggesting a listric fault found in this study for the 2008 Wells earthquake is a good example of source complexity at depth, for which there were no previous clues from surface observations. We show that both deep and shallow parts of possible listric faults can rupture in a single earthquake, which could have important implications for seismic hazard assessment in the region (Passone & Mai, 2017).

We note that our solutions consist of a relatively simple two-fault system and that ideally many planar sub-faults could be considered in our inversions to define a realistic listric, curved fault. However, as mentioned previously, even when considering three-fault configurations, the data fit only improved marginally, showing that current data sets cannot resolve such detailed faulting configurations. Future higher frequency analysis such as, for example using back projection (e.g., Ishii et al., 2005) could potentially bring further insights into the event's source process. Nevertheless, the two-fault solution found by our data-driven approach along with comparisons with aftershocks and the region's tectonics provide strong support for the rupture of both the shallow and deep parts of a likely listric fault in the region. More generally, this study forms a useful basis to study the complexity of other moderate magnitude events, which remains relatively under-studied.

## 6. Conclusions

In this study, we used a unique data set of local seismic waveforms from the USArray combined with high-quality InSAR data and teleseismic waveforms to investigate the complexity of the Mw 6.0, February 21, 2008 Wells, Nevada earthquake. The preferred two-fault solution obtained suggests a listric fault comprising a shallow (centroid depth  $\sim 4.6$  km), sub-event with Mw 5.3 and fault dip of  $\sim 77^\circ$ , and a deeper (centroid depth  $\sim 8.8$  km), larger Mw 6.0 sub-event on a subfault with shallower fault dip of  $41^\circ$ . The rupture initiated on the deeper subfault and propagated updip, with an interval of  $\sim 15$  s between the two sub-events. This is in agreement with the aftershock distribution of Smith et al. (2011). Listric faults are common in areas of extension such as the Basin and Range and thus the two-fault solution obtained in this study is consistent with the tectonics of the region. We show that ruptures can occur in both the shallow and deep parts of possible listric faults, which has key implications for seismic hazard analyses (Passone & Mai, 2017). The local USArray waveforms used in this study were key to unraveling that both shallow and deep parts of the possible listric fault slipped in the earthquake. The absence of such excellent, dense network coverage in other regions may explain why the rupture of whole listric faults has not been detected previously. They may be more common than previously thought.

## Data Availability Statement

The seismic data used in this study are freely available in the IRIS repository (<http://ds.iris.edu/ds/nodes/dmc/data/>) and the InSAR Envisat ASAR data are freely provided by the European Space Agency (ESA) and by the WInSAR/UNAVCO SAR archive: <https://earth.esa.int/web/guest/missions/esa-operational-eo-missions/envisat/instruments/asar>; <https://www.unavco.org/data/sar/sar.html>.

**Acknowledgments**

The authors thank the editor Rachel Abercrombie, the associate editor Elisa Tinti and reviewers Doug Dreger and Carl Tape for their valuable reviews, which greatly helped improve this manuscript. This research was initially supported by NERC grant NE/K005669/1 followed by NERC grant NE/N011791/1. The authors thank fruitful scientific discussions supported by the COST Action ES1401-TIDES. The authors gratefully acknowledge the availability of global seismograms from the IRIS Data Services and the II, IU, GEOSCOPE, and GEOFON networks. The seismic data analyses and inversions were carried out on the High Performance Computing Cluster supported by the Research and Computing Support services at University College London and on the national UK supercomputing facility Archer.

**References**

Agram, P. S., Jolivet, R., Riel, B., Lin, Y. N., Simons, M., Hetland, E., et al. (2013). New radar interferometric time series analysis toolbox released. *EOS, Transactions American Geophysical Union*, 94(7), 69–70. <https://doi.org/10.1002/2013EO070001>

Anderson, E. R., Zoback, M. L., & Thompson, G. A. (1983). Implications of selected subsurface data on the structural form and evolution of some basins in the northern Basin and Range province, Nevada and Utah. *The Geological Society of America Bulletin*, 94(9), 1055. [https://doi.org/10.1130/0016-7606\(1983\)94<1055:IOSSDO>2.0.CO;2](https://doi.org/10.1130/0016-7606(1983)94<1055:IOSSDO>2.0.CO;2)

Bassin, C., Laske, G., & Masters, G. (2000). The current limits of resolution for surface wave tomography in North America. *Eos Transactions American Geophysical Union*, 81(48). Abstract S12A-03.

Bevington, P. R., & Robinson, D. K. (2002). *Data reduction and error analysis for the physical sciences* (3rd ed.). McGraw-Hill.

Biasi, G. P., & Smith, K. D. (2011). *Final technical report USGS cooperative agreement for seismic network operations – western great basin seismic network operation*.

Braunmiller, J., & Nabelek, J. (1996). Geometry of continental normal faults: Seismological constraints. *Journal of Geophysical Research*, 101, 3045–3052.

Cakir, Z., & Akoglu, A. M. (2008). Synthetic aperture radar interferometry observations of the M = 6.0 Orta earthquake of 6 June 2000 (NW Turkey): Reactivation of a listric fault. *Geochemistry, Geophysics, Geosystems*, 9(8). <https://doi.org/10.1029/2008GC002031>

Chang, S.-J., Ferreira, A. M. G., Ritsema, J., van Heijst, H. J., & Woodhouse, J. H. (2015). Joint inversion for global isotropic and radially anisotropic mantle structure including crustal thickness perturbations. *Journal of Geophysical Research: Solid Earth*, 120(6), 4278–4300. <https://doi.org/10.1002/2014jb011824>

Chen, C. W., & Zebker, H. A. (2001). Two-dimensional phase unwrapping with use of statistical models for cost functions in nonlinear optimization. *Journal of the Optical Society of America A, Optics and Image Science*, 18(2), 338. <https://doi.org/10.1364/josaa.18.000338>

Crotwell, H. P., Owens, T. J., & Ritsema, J. (1999). The TauP toolkit: Flexible seismic travel-time and ray-path utilities. *Seismological Research Letters*, 70(2), 154–160. <https://doi.org/10.1785/gssrl.70.2.154>

Debayle, E., & Ricard, Y. (2012). A global shear velocity model of the upper mantle from fundamental and higher Rayleigh mode measurements. *Journal of Geophysical Research*, 117(B10). <https://doi.org/10.1029/2012JB009288>

dePolo, C. M. (2011). Building damage from the 2008 Wells, Nevada earthquake. *Nevada Bureau of Mines and Geology Special Publication*, 36, 223–326.

dePolo, C. M., & Lotspeich, D. (2011). The emergency response to the 2008 Wells, Nevada earthquake disaster. *Nevada Bureau of Mines and Geology Special Publication*, 36, 385–402.

dePolo, C. M., & Pecoraro, B. (2011). Modified Mercalli intensity maps for the February 21, 2008 Wells, Nevada earthquake. *Nevada Bureau of Mines and Geology Special Publication*, 36, 205–222.

Doser, D. I., & Smith, R. B. (1989). An assessment of source parameters of earthquakes in the cordillera of the western United States. *Bulletin of the Seismological Society of America*, 5, 1383–1409.

Dreger, D. S., Ford, S. R., & Ryder, I. (2011). Preliminary finite-source study of the February 21, 2008 Wells, Nevada earthquake. *Nevada Bureau of Mines and Geology Special Publication*, 36, 147–156.

Ekström, G., Nettles, M., & Dziewionowski, A. (2012). The global CMT project 2004–2010: Centroid-moment tensors for 13,017 earthquakes. *Physics of the Earth and Planetary Interiors*, 200–201, 1–9. <https://doi.org/10.1016/j.pepi.2012.04.002>

Farr, T. G., Rosen, P. A., Caro, E., Crippen, R., Duren, R., Hensley, S., et al. (2007). The shuttle radar topography mission. *Reviews of Geophysics*, 45(2). <https://doi.org/10.1029/2005rg000183>

Ferreira, A. M. G., Faccenda, M., Sturgeon, W., Chang, S.-J., & Schardong, L. (2019). Ubiquitous lower-mantle anisotropy beneath subduction zones. *Nature Geoscience*, 12, 301–306. <https://doi.org/10.1038/s41561-019-0325-7>

Forsyth, D. (1975). The early structural evolution and anisotropy of the oceanic upper mantle. *Geophysical Journal of the Royal Astronomical Society*, 43, 103–162. <https://doi.org/10.1111/j.1365-246X.1975.tb00630.x>

Frietsch, M., Ferreira, A., Funning, G. J., & Weston, J. (2019). Multiple fault modeling combining seismic and geodetic data: The importance of simultaneous sub-event inversions. *Geophysical Journal International*, 218(2), 958–976. <https://doi.org/10.1093/gji/ggz205>

Frietsch, M., Ferreira, A., Vales, D., & Carrilho, F. (2018). On the robustness of seismic moment tensor inversions for mid-ocean earthquakes: The azores archipelago. *Geophysical Journal International*, 215(1), 564–584. <https://doi.org/10.1093/gji/ggy294>

Funning, G. J., Parsons, B., Wright, T. J., Jackson, J. A., & Fielding, E. J. (2005). Surface displacements and source parameters of the 2003 Bam (Iran) earthquake from Envisat advanced synthetic aperture radar imagery. *Journal of Geophysical Research*, 110(B9). <https://doi.org/10.1029/2004jb003338>

Gibbs, A. D. (1984). Structural evolution of extensional basin margins. *Journal of the Geological Society*, 141(4), 609. <https://doi.org/10.1144/gsjgs.141.4.0609>

Hammond, W. C., Blewitt, G., & Kreemer, C. (2014). Steady contemporary deformation of the central basin and range province, western united states. *Journal of Geophysical Research*, 119, 5235–5253. <https://doi.org/10.1002/2014JB011145>

Hearn, E. H., & Bürgmann, R. (2005). The effect of elastic layering on inversions of GPS data for coseismic slip and resulting stress changes: Strike-slip earthquakes. *Bulletin of the Seismological Society of America*, 95(5), 1637–1653. <https://doi.org/10.1785/0120040158>

Henry, C. D., & Colgan, J. P. (2011). The regional structural setting of the 2008 Wells earthquake and Town Creek flat basin-implications for the Wells earthquake fault and adjacent structures. *Nevada Bureau of Mines and Geology Special Publication*, 36, 53–64.

Ishii, M., Shearer, P., Houston, H., & Vidale, J. (2005). Extent, duration and speed of the 2004 sumatra-andaman earthquake imaged by the hi-net array. *Nature*, 435(7044), 933–936.

Jackson, J., & McKenzie, D. (1983). The geometrical evolution of normal fault systems. *Journal of Structural Geology*, 5(5), 471–482. [https://doi.org/10.1016/0191-8141\(83\)90053-6](https://doi.org/10.1016/0191-8141(83)90053-6)

Jackson, J., & White, N. (1989). Normal faulting in the upper continental crust: Observations from regions of active extension. *Journal of Structural Geology*, 11(1–2), 15–36. [https://doi.org/10.1016/0191-8141\(89\)90033-3](https://doi.org/10.1016/0191-8141(89)90033-3)

Jonsson, S. (2002). Fault slip distribution of the 1999  $M_w$  7.1 Hector mine, California, earthquake, estimated from satellite radar and GPS measurements. *Bulletin of the Seismological Society of America*, 92(4), 1377–1389. <https://doi.org/10.1785/0120000922>

Komatitsch, D., & Tromp, J. (2002). Spectral-element simulations of global seismic wave propagation-I. Validation. *Geophysical Journal International*, 149(2), 390–412. <https://doi.org/10.1046/j.1365-246X.2002.01653.x>

Lohman, R. B. (2002). Location and mechanism of the little skull mountain earthquake as constrained by satellite radar interferometry and seismic waveform modeling. *Journal of Geophysical Research*, 107(B6). <https://doi.org/10.1029/2001jb000627>

- López-Comino, J. A., Stich, D., Ferreira, A. M. G., & Morales, J. (2015). Extended fault inversion with random slipmaps: A resolution test for the 2012  $M_w$  7.6 Nicoya, Costa Rica earthquake. *Geophysical Journal International*, 202(3), 1505–1521. <https://doi.org/10.1093/gji/ggv235>
- Marshall, G. A., Stein, R. S., & Thatcher, W. (1991). Faulting geometry and slip from co-seismic elevation changes: The 18 October 1989, Loma Prieta, California, earthquake. *Bulletin of the Seismological Society of America*, 81(5), 1660.
- McNeill, L. C., Piper, K. A., Goldfinger, C., Kulm, L. D., & Yeats, R. S. (1997). Litrict normal faulting on the Cascadia continental margin. *Journal of Geophysical Research*, 102(B6), 12123–12138. <https://doi.org/10.1029/97JB00728>
- Mendoza, C., & Hartzell, S. (2009). Source analysis using regional empirical Green's functions: The 2008 Wells, Nevada, earthquake. *Geophysical Research Letters*, 36(11), L11302. <https://doi.org/10.1029/2009GL038073>
- NASA JPL. (2013). Nasa Shuttle Radar Topography Mission Global 1 arc second. *NASA EOSDIS Land Processes DAAC*. <https://doi.org/10.5067/MEaSUREs/SRTM/SRTMGL1.003>
- Nealy, J. L., Benz, H. M., Hayes, G. P., Bergman, E. A., & Barnhart, W. D. (2017). The 2008 Wells, Nevada, earthquake sequence: Source constraints using calibrated multiple-event relocation and InSAR. *Bulletin of the Seismological Society of America*, 107(3), 1107. <https://doi.org/10.1785/0120160298>
- Okada, Y. (1985). Surface deformation due to shear and tensile faults in a half-space. *Bulletin of the Seismological Society of America*, 75(4), 1135–1154.
- Parisi, L., & Ferreira, A. M. (2016). Empirical assessment of the validity limits of the surface wave full ray theory using realistic 3-D earth models. *Geophysical Journal International*, 205(1), 146–159. <https://doi.org/10.1093/gji/ggv005>
- Passone, L., & Mai, P. M. (2017). Kinematic earthquake ground-motion simulations on listric normal faults. *Bulletin of the Seismological Society of America*, 107(6), 2980. <https://doi.org/10.1785/0120170111>
- Powell, M. J. D. (1964). An efficient method for finding the minimum of a function of several variables without calculating derivatives. *The Computer Journal*, 7(2), 155–162. <https://doi.org/10.1093/comjnl/7.2.155>
- Proffett, J. M. (1977). Cenozoic geology of the Yerington district, Nevada, and implications for the nature and origin of Basin and Range faulting. *The Geological Society of America Bulletin*, 88, 247–266.
- Ramelli, A. R., & dePolo, C. M. (2011). Quaternary faults in the 2008 Wells earthquake area. *Nevada Bureau of Mines and Geology Special Publication*, 36, 79–88.
- Savage, J. C. (1987). Effect of crustal layering upon dislocation modeling. *Journal of Geophysical Research*, 92(B10), 10595–10600. <https://doi.org/10.1029/jb092ib10p10595>
- Senturk, S., Cakir, Z., Ergintav, S., & Karabulut, H. (2019). Reactivation of the Adiyaman fault (Turkey) through the Mw 5.7 2007 Sivrice earthquake: An oblique listric normal faulting within the Arabian-Anatolian plate boundary observed by InSAR. *Journal of Geodynamics*, 131, 101654. <https://doi.org/10.1016/j.jog.2019.101654>
- Shelton, J. W. (1984). Listric normal faults: An illustrated summary. *AAPG Bulletin – American Association of Petroleum Geologists*, 68(7), 801–815.
- Smith, K., Pechmann, J., Meremonte, M., & Pankow, K. (2011). Preliminary analysis of the Mw 6.0 Wells, Nevada, earthquake sequence. *Nevada Bureau of Mines and Geology Special Publication*, 36, 127–145.
- Stein, R. S., & Barrientos, S. E. (1985). Planar high-angle faulting in the Basin and Range: Geodetic analysis of the 1983 Borah Peak, Idaho, earthquake. *Journal of Geophysical Research*, 90(B13), 11355–11366. <https://doi.org/10.1029/jb090ib13p11355>
- Stewart, J. H. (1971). Basin and Range structure: A system of horsts and grabens produced by deep-seated extension. *GSA Bulletin*, 82(4), 1019. [https://doi.org/10.1130/0016-7606\(1971\)82\[1019:BARSAS\]2.0.CO;2](https://doi.org/10.1130/0016-7606(1971)82[1019:BARSAS]2.0.CO;2)
- Tape, W., & Tape, C. (2015). A uniform parametrization of moment tensors. *Geophysical Journal International*, 202(3), 2074–2081. <https://doi.org/10.1093/gji/ggv262>
- Ward, S. N., & Barrientos, S. E. (1986). An inversion for slip distribution and fault shape from geodetic observations of the 1983, Borah Peak, Idaho, earthquake. *Journal of Geophysical Research*, 91(B5), 4909–4919.
- Wernicke, B., & Burchfiel, B. (1982). Modes of extensional tectonics. *Journal of Structural Geology*, 4(2), 105–115. [https://doi.org/10.1016/0191-8141\(82\)90021-9](https://doi.org/10.1016/0191-8141(82)90021-9)
- Weston, J., Ferreira, A. M. G., & Funning, G. J. (2011). Global compilation of interferometric synthetic aperture radar earthquake source models: 1. Comparisons with seismic catalogs. *Journal of Geophysical Research*, 116(8). <https://doi.org/10.1029/2010JB008131>
- Weston, J., Ferreira, A. M. G., & Funning, G. J. (2012). Systematic comparisons of earthquake source models determined using InSAR and seismic data. *Tectonophysics*, 532–535(0), 61–81. <https://doi.org/10.1016/j.tecto.2012.02.001>
- Weston, J., Ferreira, A. M. G., & Funning, G. J. (2014). Joint earthquake source inversions using seismo-geodesy and 3-D earth models. *Geophysical Journal International*, 198(2), 671–696. <https://doi.org/10.1093/gji/ggu110>
- Woessner, J., Schorlemmer, D., Wiemer, S., & Mai, P. M. (2006). Spatial correlation of aftershock locations and on-fault main shock properties. *Journal of Geophysical Research*, 111, B08301. <https://doi.org/10.1029/2005JB003961>
- Wright, T., Parsons, B., & Lu, Z. (2004). Toward mapping surface deformation in three dimensions using InSAR. *Geophysical Research Letters*, 31(L01607). <https://doi.org/10.1029/2003GL018827>